sensors

MDPI

Article

A Multi-Level Operation Method for Improving the Resilience of Power Systems under Extreme Weather through Preventive Control and a Virtual Oscillator

Chenghao Li [1], Di Zhang [1], Ji Han [2,*], Chunsun Tian [1], Longjie Xie [3], Chenxia Wang [2], Zhou Fang [1], Li Li [4] and Guanyu Zhang [1]

[1] Electric Power Research Institute of State Grid Henan Electric Power Company, Zhengzhou 450000, China
[2] College of New Energy, Harbin Institute of Technology at Weihai, Weihai 264209, China
[3] College of Lilac, Harbin Institute of Technology at Weihai, Weihai 264209, China; 2023211583@stu.hit.edu.cn
[4] School of Electrical Engineering and Automation, Harbin Institute of Technology, Harbin 150001, China
* Correspondence: hanji@hit.edu.cn

Abstract: This paper proposes a multi-level operation method designed to enhance the resilience of power systems under extreme weather conditions by utilizing preventive control and virtual oscillator (VO) technology. Firstly, a novel model for predicting time intervals between successive failures of the power system during extreme weather is introduced. Based on this, this paper proposes a preventive control method considering the system ramping and transmission constraints prior to failures so as to ensure the normal electricity demand within the system. Further, a VO-based adaptive frequency control strategy is designed to accelerate the regulation speed and eliminate the frequency deviation. Finally, the control performance is comprehensively compared under different experimental conditions. The results verify that the method accurately predicted the time of the line fault occurrence, with a maximum error not exceeding 3 min compared to the actual occurrence; also, the virtual oscillator control (VOC) strategy outperformed traditional droop control in frequency stabilization, achieving stability within 2 s compared to the droop control's continued fluctuations beyond 20 s. These results highlight VOC's superior effectiveness in frequency stability and control in power systems.

Keywords: virtual oscillator; resilience of power system; extreme weather; preventive control; multi-level operation

check for updates

Citation: Li, C.; Zhang, D.; Han, J.; Tian, C.; Xie, L.; Wang, C.; Fang, Z.; Li, L.; Zhang, G. A Multi-Level Operation Method for Improving the Resilience of Power Systems under Extreme Weather through Preventive Control and a Virtual Oscillator. *Sensors* **2024**, *24*, 1812. https://doi.org/10.3390/s24061812

Academic Editor: Christian Vollaire

Received: 23 January 2024
Revised: 24 February 2024
Accepted: 6 March 2024
Published: 12 March 2024

Copyright: © 2024 by the authors. Licensee MDPI, Basel, Switzerland. This article is an open access article distributed under the terms and conditions of the Creative Commons Attribution (CC BY) license (https://creativecommons.org/licenses/by/4.0/).

1. Introduction

In recent years, the escalating severity of climate change has led to an increased frequency of extreme weather events, critically impacting the operational stability of power systems [1]. For example, Texas experienced cold weather conditions in 2021, leading to the most significant load shedding in the state's history. Forty states in the US have reported longer power outages due to destructive storms, and temperatures reaching up to 40 degrees in some southern provinces of China have increased the risk to power systems due to increased electricity demand [2]. In light of the growing challenges posed by extreme weather, the study of power system resilience has become increasingly critical. Resilience refers to the system's ability to maintain operational functionality and rapidly restore system performance when facing low-probability extreme events [3]. Furthermore, confronted with challenges to power systems' resilience, it is important to develop effective methods for assessing the risk of failures and implement measures to enhance grid stability and resilience.

Numerous studies have been conducted to enhance the resilience of power systems under extreme weather conditions. Some studies have focused on evaluations of system resilience. These evaluations employ various quantification techniques to identify the

strengths and weaknesses of power systems and propose resilience enhancement strategies. For instance, one study introduced a scoring matrix to evaluate system functions from different perspectives [4], while another proposed the resilience "trapezoid" to capture critical system degradation and recovery features across different event phases [5]. Additionally, resilience has been quantified as the difference between the fully functioning system's capacity and its post-event capacity, offering a more nuanced understanding of resilience impacts [6].

In the realm of operational and planning strategies to enhance resilience, a lot of approaches have been explored. Studies have proposed probabilistic proactive generation redispatch strategies [7] and optimized recovery strategies considering distribution system reconfiguration [8]. A mixed-integer linear programming (MILP)-based method for generation redispatch during ice storms aims to strengthen resilience [9], while a three-stage decision-making methodology evaluates weighted pre-event and post-event performance losses, addressing the spatial uncertainty in fault probabilities [10]. This is complemented by innovative applications of battery energy storage systems (BESSs) for earthquake resilience [11] and the use of machine learning for fault prediction and resilience enhancement, like a distributed offline–online architecture [12] and a multiagent-based hybrid soft actor–critic (HSAC) algorithm [13]. Preventive-action-based strategies, such as multi-sensor prediction-based wide-area monitoring and control [14] and Monte Carlo simulation-based proactive unit commitment frameworks [15], are also gaining prominence in the resilience enhancement discourse.

Furthermore, the integration of renewable energy sources (RESs) has been identified as a crucial factor in augmenting power system resilience. Studies have demonstrated the efficacy of microgrid islanding in creating more resilient distribution systems [16]. A multistage restoration approach that utilizes heuristic optimization algorithms for system reconfiguration and DG islanding has been proposed [17], emphasizing the potential of RESs in emergency response scenarios. This includes approaches like transmission line switching [18], load redispatching [19], and resilience-based unit commitment [20], which collectively underscore the growing importance of RESs in enhancing the resilience of power systems against extreme weather impacts.

The aforementioned methods are crucial for enhancing the resilience of a power system, yet they have limitations. On the one hand, under extreme weather conditions, the power system may experience consecutive failures, potentially leading to insufficient local supply capabilities or even the emergence of localized power supply islands [21–23]. In such scenarios, the combined ramping capability of the generators within the local supply area and the power transmission capacity from the external grid may not be sufficient to meet the normal electricity demand within the area. However, current research primarily focuses on emergency control after power system failures, with little consideration given to the impact of potential consecutive failures before they occur. This oversight is particularly evident in the formulation of emergency dispatch strategies for power systems, where there is a lack of comprehensive integration of system ramping and transmission constraints. The system ramping constraint is critical, as it delineates the rate at which a power generator can regulate its output to match fluctuations in electricity demand, given the physical limitation on the rapidity of power output adjustment. Similarly, the transmission constraint encapsulates the capacity limitation of the power transmission network, encompassing a high-voltage transmission line and other grid components, which are pivotal in ensuring the safe and efficient transportation of electrical power without causing overheating or unacceptable voltage drops. It is important that an emergency dispatch strategy accounts for these two constraints to ensure the operational feasibility and resilience of a power system against potential failures.

On the other hand, extreme weather can lead to fragile, isolated local power supply areas with insufficient resources, poor inertia, and low disturbance resistance, threatening frequency stability. Advanced frequency regulation methods are required for their stability. The increasing presence of power electronic interfaces in power grids has enhanced

regulation flexibility. However, traditional controls like droop and virtual synchronous machine controls in power electronics, such as energy storage units, are slow to respond to disturbances, particularly in isolated power areas. Recently, virtual oscillator control (VOC) has become important for frequency regulation in power systems rich in power electronics [24,25]. VOC, using the digital control of converters, simulates LC second-order oscillation dynamics. Research on VOC aims to improve inverter performance and practical VOC applications, such as power scheduling in grid-connected modes, islanding support, and enhanced disturbance management. A challenge is balancing VOC's preference for larger inertia for angular frequency stability against the need for smaller inertia for a better active power response. Thus, a flexible, adjustable VOC beneficial for the frequency response is preferred. Additionally, developing a VOC-based controller that minimizes frequency errors is necessary.

To address the aforementioned issues, this paper proposes a multi-level operation method for improving the resilience of power systems under extreme weather through preventive control and a VO. The new contributions can be summarized as follows:

1. This paper introduces a novel method of preventive control for power systems, particularly focusing on the power constraints between successive failures. This method is significant, as it considers both the combined ramping capability of generators within the local supply area and the power transmission capacity from the external grid before the occurrence of successive failures. This approach is designed to ensure that the normal electricity demand within the local supply area is met, even in the face of potential disruptions. Such a preventive control mechanism is innovative in its comprehensive approach to power system resilience, especially in scenarios of extreme weather and high-risk conditions for cascading failures.
2. The paper proposes a VOC-based adaptive frequency control strategy for power systems. A key element of innovation here is the dynamic adjustment of the VOC loop coefficients according to the system's operating conditions during transient states. This adaptive strategy marks a significant advancement over traditional VOC implementations, where coefficients are usually static. By dynamically adjusting the VOC loop coefficients, this method enhances the frequency recovery rate, offering a more responsive and efficient approach to frequency regulation under varying system conditions.

The rest of this paper is organized as follows. In Section 2, an upper-level preventive control method that considers successive failures is presented. Section 3 presents a lower-level control method based on a VO to accelerate the frequency regulation speed. A case study is provided in Section 4. Section 5 concludes the paper.

2. Upper-Level Preventive Control Considering Successive Failures

Extreme weather can potentially lead to the successive tripping of multiple power lines, and the whole power system might be partitioned into relatively independent regions and even several isolated regions. In this circumstance, some regions may not have an abundant power supply due to the ramping limits of generators and the limited power transmission capacity of lines. This upper-level control framework aims to ensure that the combined capability of the ramping up of generators within the local supply region and the power transmission capacity from the external grid are greater than the load within the local supply region.

During the fault process, the transmission system needs to redispatch generators after the occurrence of faults in order to meet the security conditions of the system under successive failures. The objective function is firstly established according to the dynamic situation of the power system, as shown in (1). The objective function aims to minimize the

cost of electricity generation as much as possible while also ensuring minimal variation in the system's states (voltage and phase angle) before and after any faults.

$$\min C = \sum_{m=1}^{N_G} c_{Gm}|P_{Gm,t}| + \sum_{m=1}^{N_E} c_{Em}|P_{Em,t}| + |z_t - h(x_t)| \tag{1}$$

where $P_{Gm,t}$ is the active power of the m-th generator at time t. c_{Gm} is the cost coefficient of the m-th generator. N_G is the number of generators. $P_{Em,t}$ is the active power of the m-th energy storage unit at time t. c_{Em} is the cost coefficient of the m-th energy storage unit. N_E is the number of energy storage units. z_t represents the measurement vector including the bus voltage magnitude $V_{i,t}$ ($i \in \Omega_B$, and Ω_B is the set of system buses) and phase angle deviation θ_{ij} ($i \in \Omega_B$, $j \in \Omega_B$) before the occurrence of the fault. $h(x_t)$ is the fault state vector including the bus voltage magnitude $V_{i,t}$ ($i \in \Omega_B$, and Ω_B is the set of system buses) and phase angle deviation θ_{ij} ($i \in \Omega_B$, $j \in \Omega_B$) after the occurrence of the fault.

Furthermore, in the method of preventive control, it is necessary to consider the following constraints:

(1) Power flow constraint: The power system must satisfy the power flow equations, and the line flow should be within the prescribed limits [26].

$$\begin{cases} P_{Gi,t}^{all} - P_{Di,t}^{all} = \sum\limits_{j \in \Omega_B} V_{i,t}V_{j,t}(G_{ij}\cos\theta_{ij,t} + B_{ij}\sin\theta_{ij,t}) \\ Q_{Gi,t}^{all} - Q_{Di,t}^{all} = \sum\limits_{j \in \Omega_B} V_{i,t}V_{j,t}(G_{ij}\sin\theta_{ij,t} - B_{ij}\cos\theta_{ij,t}) \end{cases} \tag{2}$$

$$\begin{cases} P_{ij,t} = -(V_{i,t})^2 G_{ij} + V_{i,t}V_{j,t}(G_{ij}\cos\theta_{ij,t} + B_{ij}\sin\theta_{ij,t}) \\ Q_{ij,t} = -(V_{i,t})^2 B_{ij} + V_{i,t}V_{j,t}(G_{ij}\sin\theta_{ij,t} - B_{ij}\cos\theta_{ij,t}) \\ P_{ij,\min} \le P_{ij,t} \le P_{ij,\max} \\ Q_{ij,\min} \le Q_{ij,t} \le Q_{ij,\max} \end{cases} \tag{3}$$

where $P_{Gi,t}^{all}$ and $Q_{Gi,t}^{all}$ are the active and reactive power injected into bus i of all kinds of generation systems, including generators, energy storage units, wind power systems, etc. $P_{Di,t}^{all}$ and $Q_{Di,t}^{all}$ are the active and reactive power demands at bus i of all kinds of loads. $P_{ij,t}$ and $Q_{ij,t}$ are the active and reactive power from the i-th bus to the j-th bus. G_{ij} and B_{ij} represent the admittance parameter between transmission line ij. $P_{ij,\max}$ and $P_{ij,\min}$ represent the active power limits of transmission line ij. $Q_{ij,\max}$ and $Q_{ij,\min}$ denote the reactive power limits of transmission line ij.

(2) System reserve constraint: The system needs positive and negative spinning reserve capacity to mitigate the impact of uncertainties in wind power and load forecasting, thus ensuring the security and stability of the system operation.

$$\begin{cases} \sum\limits_{i=1}^{N_G} R_{Gi,t}^{up} + \sum\limits_{i=1}^{N_E} R_{Ei,t}^{up} \ge \varepsilon_L \cdot P_{Load,t} + \varepsilon_W \cdot P_{fW,t} \\ \sum\limits_{i=1}^{N_G} R_{Gi,t}^{down} + \sum\limits_{i=1}^{N_E} R_{Ei,t}^{down} \ge \varepsilon_L \cdot P_{Load,t} + \varepsilon_W \cdot P_{fW,t} \end{cases} \tag{4}$$

where ε_L and ε_W represent the proportional forecasting errors of the system load and wind power, respectively. $R_{Gi,t}^{up}$ and $R_{Gi,t}^{down}$ denote the positive/negative spinning reserve capacity of generator i at time t. $R_{Ei,t}^{up}$ and $R_{Ei,t}^{down}$ denote the positive/negative spinning reserve capacity of energy storage unit i at time t. $P_{Load,t}$ denotes the total load within the system, while $P_{fW,t}$ denotes the forecasted wind power output.

(3) Constraints on the operation of the generator: These encompass the constraints on the output, the ramping constraints, the startup and shutdown times, and the reserve constraints of generators.

$$P_{Gi,\min} \le P_{Gi,t} \le P_{Gi,\max} \tag{5}$$

$$\begin{cases} T_{\mathrm{G}i,t}^{\mathrm{on}} \geq T_{\mathrm{G}i,\min}^{\mathrm{on}} \\ T_{\mathrm{G}i,t}^{\mathrm{off}} \geq T_{\mathrm{G}i,\min}^{\mathrm{off}} \\ P_{\mathrm{G}i,t+1} - P_{\mathrm{G}i,t} \leq v_{\mathrm{Ramp,G}i}^{\mathrm{up}} \cdot \Delta t \\ P_{\mathrm{G}i,t} - P_{\mathrm{G}i,t+1} \leq v_{\mathrm{Ramp,G}i}^{\mathrm{down}} \cdot \Delta t \end{cases} \tag{6}$$

$$\begin{cases} P_{\mathrm{G}i,t} + R_{\mathrm{G}i,t}^{\mathrm{up}} \leq P_{\mathrm{G}i,\max} \\ 0 \leq R_{\mathrm{G}i,t}^{\mathrm{up}} \leq v_{\mathrm{Ramp,G}i}^{\mathrm{up}} \cdot \Delta t \\ P_{\mathrm{G}i,t} - R_{\mathrm{G}i,t}^{\mathrm{down}} \geq P_{\mathrm{G}i,\min} \\ 0 \leq R_{\mathrm{G}i,t}^{\mathrm{down}} \leq v_{\mathrm{Ramp,G}i}^{\mathrm{down}} \cdot \Delta t \end{cases} \tag{7}$$

where $P_{\mathrm{G}i,\max}$ and $P_{\mathrm{G}i,\min}$, respectively, denote the upper and lower limits of the active power output of generator i. $T_{\mathrm{G}i,t}^{\mathrm{on}}$ represents the startup time of generator i during time period t, while $T_{\mathrm{G}i,t}^{\mathrm{off}}$ represents the shutdown time of generator i during time period t. $T_{\mathrm{G}i,\min}^{\mathrm{on}}$ denotes the minimum allowable startup time for generator i, and $T_{\mathrm{G}i,t}^{\mathrm{off}}$ represents the minimum allowable shutdown time for generator i. $v_{\mathrm{Ramp,G}i}^{\mathrm{up}}$ and $v_{\mathrm{Ramp,G}i}^{\mathrm{down}}$ represent the upward and downward ramp rates of generator i, respectively. Δt denotes the minimum scheduling period.

(4) Constraints on the operation of the energy storage unit: These encompass constraints on the reserve and capacity of energy storage units.

$$\begin{cases} 0 \leq R_{\mathrm{E}i,t}^{\mathrm{up}} \leq P_{\mathrm{N,E}i} - P_{\mathrm{E}i,t} \\ 0 \leq R_{\mathrm{E}i,t}^{\mathrm{down}} \leq P_{\mathrm{E}i,t} + P_{\mathrm{N,E}i} \end{cases} \tag{8}$$

$$\begin{cases} E_{\min,i} \leq E_{t,i} - (P_{\mathrm{E}i,t} + R_{\mathrm{E}i,t}^{\mathrm{up}})/\eta_i \leq E_{\max,i} \\ E_{\min,i} \leq E_{t,i} - (P_{\mathrm{E}i,t} - R_{\mathrm{E}i,t}^{\mathrm{down}})/\eta_i \leq E_{\max,i} \end{cases} \tag{9}$$

where $P_{\mathrm{N,E}i}$ represents the rated power of energy storage unit i, while $E_{\min,i}$ and $E_{\max,i}$ represent the minimum and maximum energy capacities of storage unit i. η_i represents the charge or discharge efficiency of storage unit i.

(5) Power constraint between successive failures: Following a power system failure, isolated operation in certain regions or limited interconnection with the rest of the large power grid may ensue. In such scenarios, the affected area may experience insufficient generation capacity. In particular, in the intervals between consecutive failures, without a well-orchestrated generation plan, generators within the region may struggle to swiftly adjust their output to anticipate the next contingency. Additionally, due to transmission constraints, the remainder of the large power grid may be unable to supply adequate power to this area, thereby increasing the risk of widespread power outages in the power system.

We utilize Figure 1 for a more intuitive explanation. Assuming that Node 9 bears a substantial load at time t_0 while Node 3 exhibits a limited generation level at the same time, at this juncture, the load at Node 9 will be sustained by Lines 3–9, 6–9, and 8–9. Furthermore, employing the approach outlined in Section 2, if it is possible to forecast the occurrence of faults on Lines 6–9 and 8–9, and the time of occurrence for each fault is denoted by t_1 and $t_1 + K\Delta t$, respectively, it becomes evident that, following the fault on Line 6–9, the load at Node 9 will be supported by Lines 3–9 and 8–9. Subsequently, after the fault on Line 8–9, the load at Node 9 can only be supplied by Line 3–9. If the ramping capability of the generator at Node 3 is insufficient to meet the load requirement at Node 9 at time $t_1 + K\Delta t$, it becomes necessary for Node 9 to curtail a portion of its load to maintain supply–demand equilibrium. One potential resolution is to preemptively increase the output of the generator at Node 3 upon forecasting the fault occurrences on Lines 6–9 and 8–9 at times t_1 and $t_1 + K\Delta t$, thereby mitigating Node 9's reliance on Lines 6–9 and 8–9 for supply and ensuring that the generator's output at Node 3 is able to ramp up to meet the load requirements at times t_1 and $t_1 + K\Delta t$.

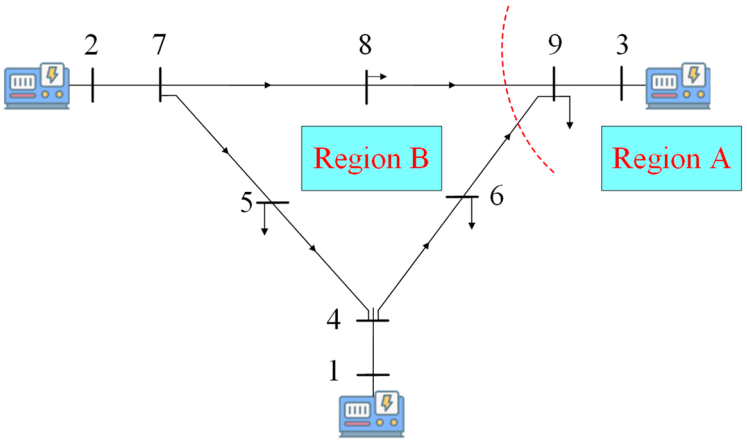


Figure 1. The pre-control process of power flow in a transmission section.

Based on the aforementioned analysis, the power constraint between successive failures is set as follows:

$$\begin{cases} \sum\limits_{i\in\Omega_{\mathrm{ISO}}}(P_{\mathrm{G}i,t}+R^{\mathrm{up}}_{\mathrm{G}i,t})+\sum\limits_{ij\in\Omega_{\mathrm{CON}}}P_{ij,\max}\geq\sum\limits_{i\in\Omega_{\mathrm{ISO}}}P^{\mathrm{all}}_{\mathrm{D}i,t} \\ \sum\limits_{i\in\Omega_{\mathrm{ISO}}}(P_{\mathrm{G}i,t+1}+R^{\mathrm{up}}_{\mathrm{G}i,t+1})+\sum\limits_{ij\in\Omega_{\mathrm{CON}}}P_{ij,\max}\geq\sum\limits_{i\in\Omega_{\mathrm{ISO}}}P^{\mathrm{all}}_{\mathrm{D}i,t+1} \\ \cdots \\ \sum\limits_{i\in\Omega_{\mathrm{ISO}}}(P_{\mathrm{G}i,t+K}+R^{\mathrm{up}}_{\mathrm{G}i,t+K})+\sum\limits_{ij\in\Omega_{\mathrm{CON}}}P_{ij,\max}\geq\sum\limits_{i\in\Omega_{\mathrm{ISO}}}P^{\mathrm{all}}_{\mathrm{D}i,t+K} \end{cases} \tag{10}$$

where K represents the time interval between adjacent failures. Ω_{ISO} denotes the set of nodes in the local power supply area, while Ω_{CON} signifies the set of lines connected to the local power supply area.

The equation illustrates that, following a failure, the power system may be partitioned into relatively independent regions. It is imperative to ensure that, during the occurrence of a failure, the load within the local power supply area remains unaffected. Specifically, the combined ramping capability of the generators within the local supply area and the power transmission capacity from the external grid must be sufficient to meet the normal electricity demand within the area.

(6) Constraint on renewable energy output: The actual dispatch output of wind power must not exceed the forecasted wind power output.

$$0\leq P_{\mathrm{sW},t}\leq P_{\mathrm{fW},t} \tag{11}$$

where $P_{\mathrm{sW},t}$ represents the actual output of wind power.

To sum up, the power flow and generator/energy storage system operation constraints are critical for ensuring that the physical operation of the power system adheres to technical specifications and limits. The constraints of the system reserve and power stability between failures are vital for preparing the system against uncertainties (like wind power and load forecasting errors) and for maintaining stability and continuous operation in the aftermath of system failures, ensuring that there is sufficient generation capacity and strategic operation planning to avoid widespread outages. The constraint on renewable energy output focuses on aligning the actual renewable power dispatch with forecasted outputs. By combining the above six constraints and the objective function, the upper-level preventive control scheme considering successive failures can be obtained.

Notably, in the preventive control optimization process, we utilize a differential evolution–particle swarm optimization (DE-PSO) algorithm [27]. The DE-PSO algorithm, merging differential evolution (DE) and particle swarm optimization (PSO), excels in optimizing complex problems without easily getting trapped in local optima. Its hybrid

nature combines DE's global search with PSO's swift convergence, enabling the effective exploration and exploitation of the search space. This makes DE-PSO particularly adept at handling problems with numerous constraints, as it can adaptively balance between exploring new areas and refining existing solutions. Thus, DE-PSO stands out for its ability to navigate challenging optimization landscapes and find high-quality solutions amidst a multitude of constraints. Considering the dynamic and often rapidly changing conditions of power systems during extreme weather events, the optimization is set to recur at intervals of 15 min. This interval is optimal for updating the system's preventive strategies in response to evolving environmental and operational conditions, thereby enhancing the system's adaptability and resilience against cascading failures. Testing indicates that the PSO algorithm can complete an optimization cycle in approximately 10 s, and this duration is acceptable and ensures a balance between computational expediency and precision.

3. Lower-Level Control Based on Virtual Oscillator

On short time scales, the stochastic nature of the load and renewable energy sources may influence the stability of the system frequency, especially when the power system is divided into relatively independent regions due to faults. This section (Section 3) explores the rapid adjustment characteristics of power electronic devices of energy storage devices and proposes a frequency control method for power systems based on a VO.

Firstly, the integration of VOC into a multi-level frequency control architecture marks a significant advancement for power systems, particularly those rich in power electronics. This approach represents a pioneering step in harmonizing VOC strategies with contemporary power system control requirements. Secondly, we developed an innovative frequency regulation method using the VOC strategy. This method utilizes a rapid time-domain model in conjunction with coupling droop characteristics, enabling VOC-controlled inverters to measure frequency without the need for a Phase-Locked Loop (PLL). This advancement significantly reduces the computational load, enhancing the efficiency of the system. Thirdly, this manuscript details a novel methodology for optimizing VOC parameters, including virtual capacitance and inductance. This optimization is crucial for dynamically adjusting system parameters in response to real-time operational conditions, thereby improving the frequency regulation performance of power systems [28].

3.1. Characteristic Analysis of VOC Inverter

Figure 2 depicts a typical VOC inverter of the Van der Pol (VdP) type, comprising a VdP type of VO, DG, and an inverter. The circuit model of the VdP type of VO consists of three parallel parts: (1) an LC resonance loop that can generate a resonant frequency and whose oscillation characteristics are reflected in the bidirectional energy flow between a virtual capacitor and a virtual inductor; (2) a negative impedance, which is essential to the system's transient process and closely related to the inertial frequency regulation scale; (3) a voltage-controlled current source.

The dynamics of VOC are given by [29]

$$\begin{cases} \frac{\mathrm{d}i_L}{\mathrm{d}t} = \frac{v_\mathrm{c}}{L} \\ \frac{\mathrm{d}v_\mathrm{c}}{\mathrm{d}t} = -\frac{\alpha}{C}v_\mathrm{c}^3 + \frac{\sigma}{C}v_\mathrm{c} - \frac{1}{C}i_L - \frac{\kappa_i}{C}i \end{cases} \tag{12}$$

where i_L is the inductor current. v_c is the capacitor voltage. C, L, and σ are the virtual capacitance, inductance, and conductance, and the nonlinear voltage-dependent current source is parameterized by α. The controller is interfaced via voltage and current scaling values, κ_v and κ_i.

From Figure 2, the output voltage command is

$$v = \kappa_v(v_C\cos\Phi - \varepsilon i_L\sin\Phi) \tag{13}$$

where $\varepsilon = \sqrt{L/C}$, and Φ is a fixed user-defined angle, typically set to either 0 or $\pi/2$, which specifies the type of droop-like characteristic that the VO-controlled inverter exhibits in the steady state.

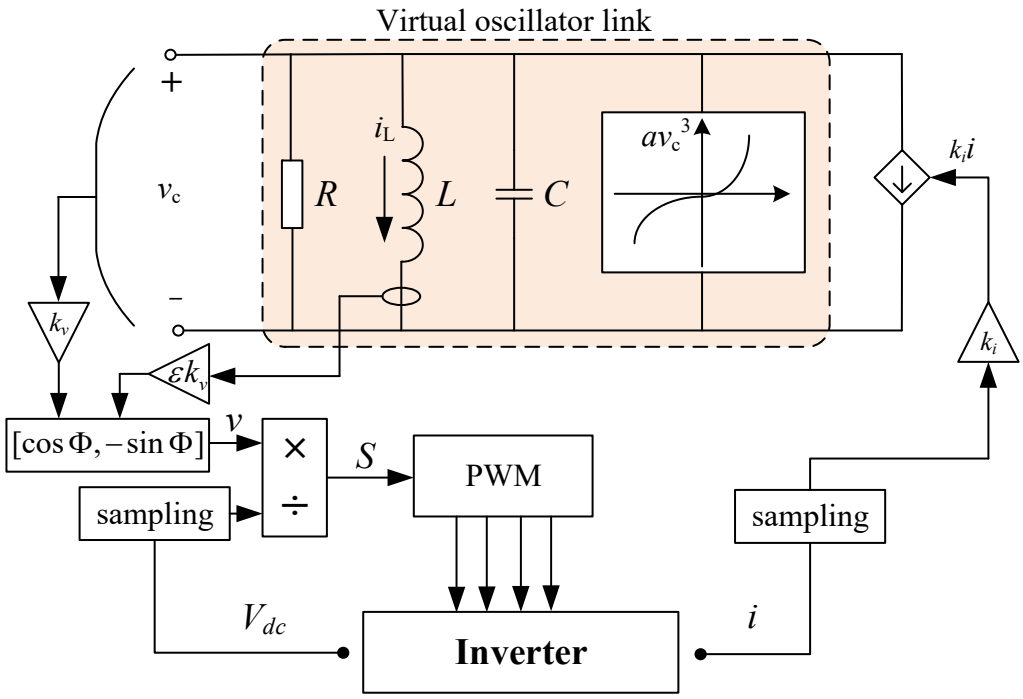


Figure 2. The VdP type of VO.

Further, assuming $\Phi = \pi/2$, an averaged model is utilized by averaging the trajectory of the oscillator over one ac cycle, and then we can obtain the following amplitude and frequency dynamics:

$$\frac{\mathrm{d}\overline{\theta}^*}{\mathrm{d}t} = -\frac{\kappa_v \kappa_i}{6C\overline{V}^2} P \tag{14}$$

where P is the average three-phase real power over one cycle $\omega^*/2\pi$.

Given (14) and the fact that $\theta(t) + \omega t = \theta^*(t) + \omega^* t$ and $\mathrm{d}\theta/\mathrm{d}t = 0$ in the steady state, we have

$$\omega_{\mathrm{eq}} = \omega^* - \frac{\kappa_v \kappa_i}{2C\overline{V}_{\mathrm{oc}}^2} P_{\mathrm{eq}} \tag{15}$$

This VOC inverter uses symmetrical pulse-width modulation (SPWM) in the control. A reference signal (usually a sine-wave signal) is compared with a high-frequency triangular-wave signal, and the on-time of the switching device is controlled according to the comparison results.

Assuming that the reference signal is V_{ref} and the high-frequency triangular-wave signal is V_{tri}, their comparison yields a result. If $V_{\mathrm{ref}} > V_{\mathrm{tri}}$, the switching device conducts; if $V_{\mathrm{ref}} < V_{\mathrm{tri}}$, the switching device turns off.

By controlling the conduction time of the switching devices, the output voltage can be regulated. The longer the conduction time, the higher the output voltage; the shorter the conduction time, the lower the output voltage. Specifically, an SPWM signal can be derived from the comparison of V_{ref} and V_{tri} to control the conduction time of the switching devices. This modulation signal can be described by the following formula:

$$D = \frac{V_{\mathrm{ref}}}{V_{\mathrm{tri}}} \times 100\% \tag{16}$$

where D is the duty cycle representing the percentage of conduction time in the total period, V_{ref} represents the reference signal, and V_{tri} represents the triangular-wave signal. By controlling this duty cycle, the precise adjustment of the output voltage can be achieved, thus realizing SPWM control.

The converters based on VOC exhibit deviations from their nominal responses, which vary depending on the active power. These deviations are characterized by the slope of the droop curves, indicating that VOC droop characteristics are embedded in its nonlinear dynamics model. As a result, VOC has the primary frequency regulation characteristics of droop control. The VOC time-domain model is rapid, and when combined with its coupling droop characteristics, it enables the measurement of frequency without requiring the use of a Phase-Locked Loop (PLL). This feature significantly reduces the calculation burden of the controller. Additionally, the primary frequency regulation scale of VOC is shorter than that of droop control, allowing for faster attainment of the steady state.

3.2. Control Method

3.2.1. Overall Framework

This paper proposes a multi-level frequency control architecture suitable for a VOC strategy in power systems, as depicted in Figure 3. The proposed architecture consists of two levels: lower-level primary frequency control and upper-level secondary frequency control. At the lower level, a multistage frequency regulation architecture is used with VOC to achieve frequency regulation. Additionally, a virtual link is added to compensate for lower inertia power, and the dynamic adjustment of the virtual capacitance is performed to optimize the inertia of the frequency regulation dimension. To facilitate information interaction between distributed generation units, network layer communication is utilized.

3.2.2. Determination of Virtual Capacitance

Figure 4 shows the transient frequency characteristics of the power system before and after optimal inertia frequency regulation optimization. The red curve is the frequency characteristics before optimization, and the blue curve is the frequency characteristics after optimization. Time scales t_1 and t_3 are the frequency dip and frequency recovery scales before optimization, while time scales t_2 and t_4 are the frequency dip and frequency recovery scales after optimization, respectively. At the scale of t_1 or t_2, the frequency change rate rises sharply after the disturbance appears and gradually decreases within this time scale. However, at the t_3 or t_4 scale, the frequency change rate gradually increases. This paper expects a longer frequency drop process with a smaller frequency deviation, that is, $t_2 > t_1$ and $\Delta f_2 < \Delta f_1$. Also, the frequency recovery process is expected to be faster, that is, $t_4 < t_3$.

Based on the analysis of the influence of VOC parameters on the control transient characteristics in Appendix B, it was found that virtual capacitance plays a crucial role and has a proportional relationship with the transient response time. In order to achieve the ideal optimization effect, the value of virtual capacitance should be larger during the frequency drop stage but smaller during the frequency recovery stage. To meet the requirements for inertia frequency regulation optimization, an adaptive virtual inertia control strategy based on the dynamic change in VOC parameters is proposed in this article, which is

$$\begin{cases} C_{inertia} = k_J \frac{|\omega-\omega_0|}{\omega-\omega_0} \frac{d\Delta\omega}{dt} \\ C_{con} = C_0 + C_{inertia} \\ L = \frac{1}{C(\omega_0)^2} \end{cases} \tag{17}$$

where $C_{inertia}$ is the value of the virtual compensation capacitance. C_0 is the initial value of the virtual capacitor. C_{con} is the final virtual capacitance value. $\Delta\omega$ is the frequency variation. ω_0 is the rated angular frequency. k_J is the inertia compensation coefficient.

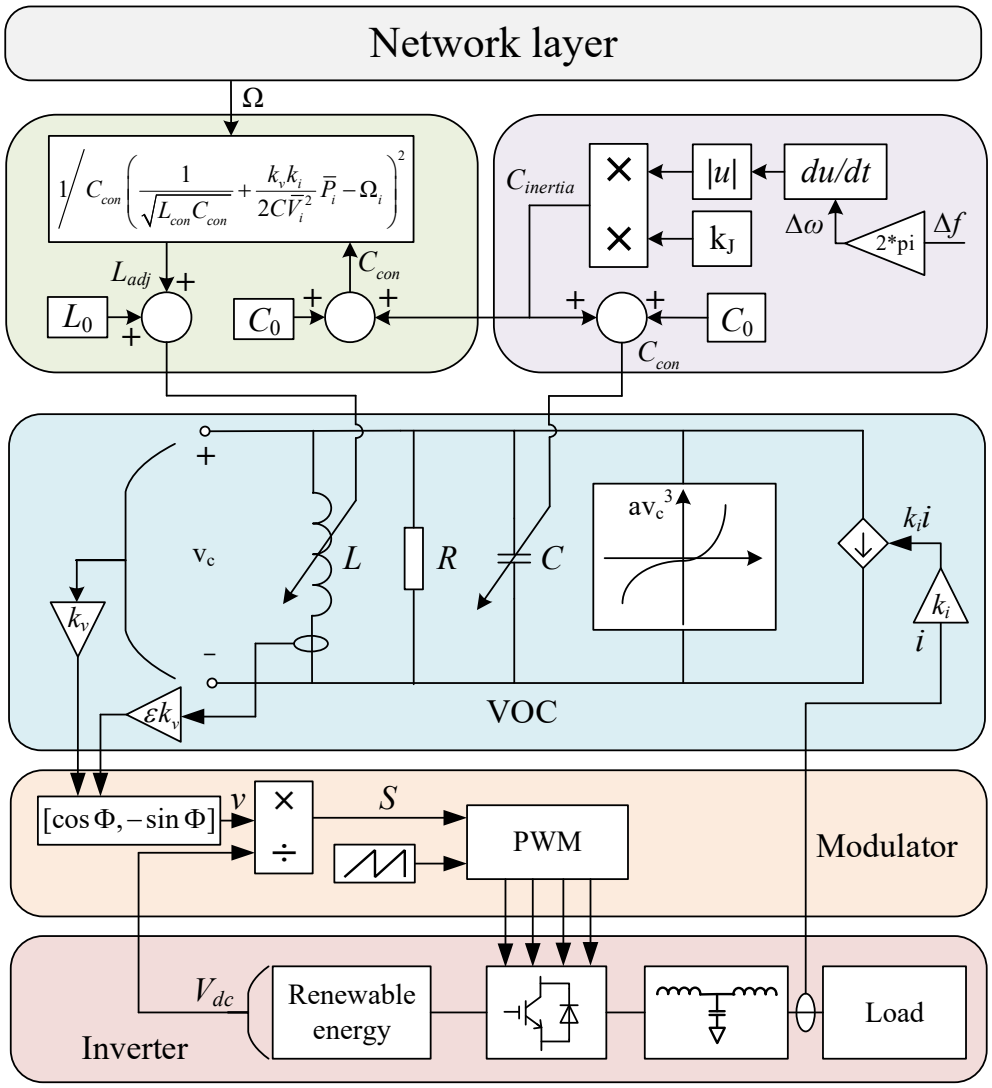


Figure 3. Multi-level control architecture of power system.

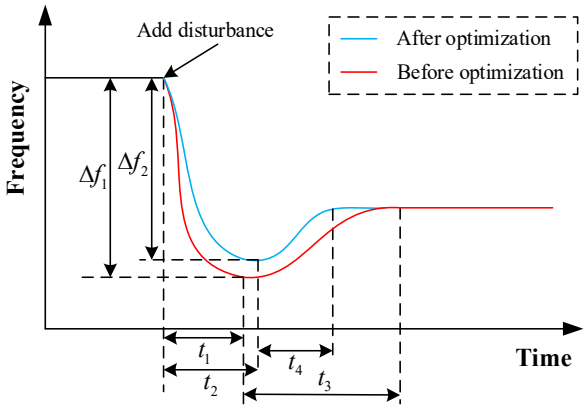


Figure 4. Comparison of transient frequency characteristics of power system before and after ideal inertia optimization.

By substituting (16) into Equation (15), the following equations can be obtained:

$$\frac{2(C_0 + C_{inertia})\overline{V}_{oc}^2}{k_v k_i}\left(\omega - \omega^*\right) = P_{out} \tag{18}$$

$$\frac{2C_{inertia}\overline{V}_{oc}^2}{k_v k_i}\left(\omega-\omega^*\right)=P_{out}-\frac{2C_0\overline{V}_{oc}^2}{k_v k_i}\left(\omega-\omega^*\right) \tag{19}$$

Equation (17) represents the active power frequency sag equation of VOC, with the right side showing the coupling effect between active power and frequency, while the left side represents the superimposed virtual inertia power. The adaptive control method of virtual inertia allows for the automatic adjustment of the virtual capacitance based on changes in frequency variation. When the frequency change rate is high, a higher value of virtual capacitance can be set to increase the transient response time and reduce the frequency change rate simultaneously. As the frequency approaches stability, the frequency change rate gradually decreases, and the value of the virtual capacitance decreases accordingly, thus accelerating the transient response speed of the system.

3.2.3. Determination of Virtual Inductor

In Appendix B, we analyze the coupling droop characteristics of the VOC inverter, and here, we assume that the coupling droop relation of active power and frequency is

$$\begin{cases} \omega_i=\omega^*-m_{P-\omega}\overline{P}_i \\ m_{P-\omega}=\frac{k_v k_i}{2C_{con}\overline{V}_{oc}^2} \end{cases} \tag{20}$$

where $m_{P-\omega}$ is the droop coefficient. ω_i is the angular frequency for node i. $\overline{P}_i$ is the active power of node i. ω^* is the rated angular frequency.

As shown in (19), the droop coefficient of VOC is determined by the VOC parameters. Therefore, dynamically adjusting the VOC parameters can be used to adjust the frequency characteristics of a power system. Based on sparse communication networks, the upper-level control should be incorporated into dynamically adjustable VOC parameters. Assuming that the power-generating unit acts as a node, the adjacency matrix A forms a communication network connection between nodes i and j, with its elements $a_{ij}=a_{ji}>0$ describing the network's communication status. The upper-level frequency control based on VOC and consensus theory is as follows:

$$\omega_i=\omega^*+\frac{k_v k_i}{2C_{con}\overline{V}_{oc}^2}\overline{P}_i-\Omega_i \tag{21}$$

$$\frac{d\Omega_i}{dt}=-g_f\left(\omega_i-\omega^*\right)-\sum_{j=1}^{n}a_{ij}\left(\Omega_i-\Omega_j\right) \tag{22}$$

where Ω_i is the control variable of the frequency controller. g_f is the positive gain that affects the frequency adjustment speed of node i. a_{ij} is the positive gain that affects the power-sharing rate between nodes i and j.

According to consensus theory, the state variables of both Ω_i and Ω_j will eventually converge to the same value. Specifically, each node of the droop characteristic curve will move by the same amount, $\omega_i-\omega_0$, as depicted in Figure 5. Therefore, there is an agreement in the change in droop characteristics across all nodes.

When the system reaches a steady state, the derivative on the left-hand side of (21) becomes zero. This is also the point where the frequency deviation in (21) equals zero, which means that the system frequency and the rated angular frequency are equal to each other. Therefore, the system regulation achieves no difference, i.e., $\omega_i=\omega^*$. To control the upper-level controller, the VOC parameter is introduced, and the virtual capacitor C remains unchanged. On the other hand, the virtual inductor L can be adjusted, which results in the system frequency being determined by the adjustable virtual inductor L_{adj}. Based on the adjustable virtual inductor L_{adj}, the system frequency is

$$\omega_i=\frac{1}{\sqrt{L_{adj}C_{con}}} \tag{23}$$

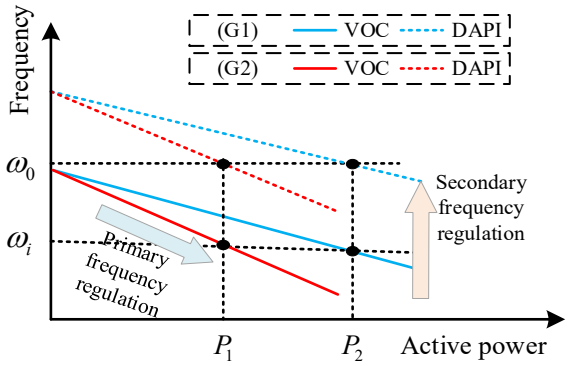


Figure 5. The secondary frequency regulation process based on the VOC droop curve.

Assuming that the parameters of the LC resonance loop are L_{con} and C_{con} when the system frequency is the rated value, by substituting (22) into (20), one can obtain

$$L_{adj} = 1/C_{con}\left(\frac{1}{\sqrt{L_{con}C_{con}}} + \frac{k_v k_i}{2C\overline{V}_i^2}\overline{P}_i - \Omega_i\right)^2 \tag{24}$$

As can be seen from (23), the control variable Ω_i of the controller is absorbed into the coupling droop characteristics of VOC through the adjustable inductance of the VO controller. When the system reaches a steady state, the adjustable inductance L_{adj} value will tend to be L_{con}, and the frequency ω_i will also tend to be the rated frequency $\omega*$.

4. Case Study

4.1. System Description

This paper utilized the IEEE-39 power system in the simulation experiments. This system comprises 38 transmission lines, 10 generators, 3 wind farms, and 6 energy storage units. A detailed visualization of the power system is presented in Figure 6. The parameters of the generators are listed in Table 1. It is assumed that the wind speed in the wind farm follows a Weibull distribution, and the scale factor, shape factor, cut-in wind speed, rated wind speed, and cut-out wind speed are listed in Table 2. The parameters of the energy storage units are listed in Table 3. VOC is employed in the inverters of the energy storage units, and they are coordinated through the cyber network layer shown in Figure 7. The parameter settings of the VO controllers for the energy storage units are listed in Table 4.

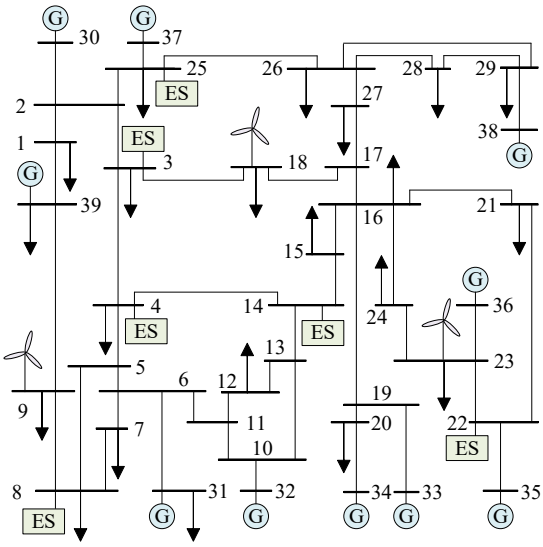


Figure 6. Topology diagram of power system.

Table 1. Parameters of the generators.

Parameter Symbol	Parameter Name and Unit	Value									
		Node 30	**Node 31**	**Node 32**	**Node 33**	**Node 34**	**Node 35**	**Node 36**	**Node 37**	**Node 38**	**Node 39**
P^*	Upper limit of active power (MW)	1040	646	725	652	508	687	580	564	865	1100
P^*	Lower limit of active power (MW)	0	0	0	0	0	0	0	0	0	0
Q^*	Upper limit of reactive power (Mvar)	400	300	300	250	167	300	240	250	300	300
Q^*	Lower limit of reactive power (Mvar)	140	−100	150	0	0	−100	0	0	−150	−100

Table 2. Parameters of the wind farms.

Parameter Symbol	Parameter Name and Unit	Value		
		Node 9	**Node 18**	**Node 23**
P^*	Capacity (MW)	500	400	450
Q^*	Scale factor	10.7	8.7	10
L_f	Shape factor	3.97	4.7	4.2
L_g	Cut-in wind speed (m/s)	3.5	3.5	3.5
C_f	Rated wind speed (m/s)	15	15	15
$\|\Delta\omega\|_{max}$	Cut-out wind speed (m/s)	25	25	25

Table 3. Parameters of the energy storage units.

Parameter Symbol	Parameter Name and Unit	Value					
		Node 3	**Node 4**	**Node 8**	**Node 14**	**Node 22**	**Node 25**
P^*	Rated active power (MW)	200	300	250	350	200	100
Q^*	Rated reactive power (Mvar)	20	30	25	35	20	10
L_f	(μH)	300	240	400	300	240	400
L_g	(μH)	300	240	400	300	240	400
C_f	(μF)	20	20	20	20	20	20
R_d	(Ω)	1.5	1.5	1.5	1.5	1.5	1.5
ω_0	Rated angular velocity (rad/s)	100π	100π	100π	100π	100π	100π
$\|\Delta\omega\|_{max}$	Maximum angular velocity offset (rad/s)	π	π	π	π	π	π

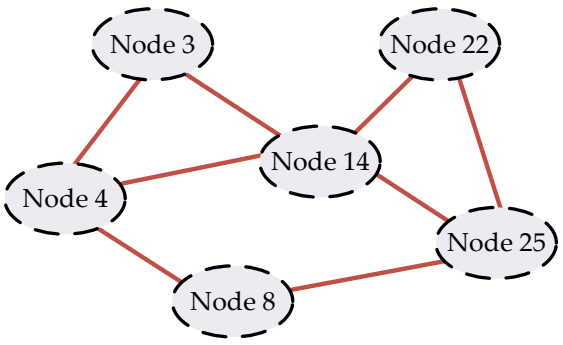


Figure 7. Cyber connection of the energy storage units.

Table 4. Parameter settings of the VO controllers for the energy storage units.

Parameter Symbol	Parameter Name	Value	Unit
k_v	Voltage proportionality factor	110	-
σ	Negative impedance	5.0868	Ω^{-1}
α	Cubic current source coefficient	3.414	A/V^3
L_0		58.9	μH
C_0		119.3	mF
k_{i1}	The first current scaling factor	0.152	-
k_{i2}	The second current scaling factor	0.304	-
k_{i3}	The third current scaling coefficient	0.456	-

4.2. Verification of Upper-Level Preventive Control

Suppose that high wind occurs at 9:00 throughout the power system, causing Line 14–15, Line 9–39, and Line 3–4 trips in succession. This results in the isolated operation of the local power grid, as shown in the following Figure 8. The occurrence process of successive failures that is measured in the actual power system is as follows:

(1) At 9:28, Line 14–15 is broken and fails to reclose;
(2) At 10:02, Line 9–39 is broken and fails to reclose;
(3) At 10:42, Line 3–4 is broken and fails to reclose, and the whole power system is separated into two regions, as shown in Figure 8.

To verify the effectiveness of the model of successive failures in the power system, this whole successive failure process is modeled by the proposed method according to Equations (A2) and (A3).

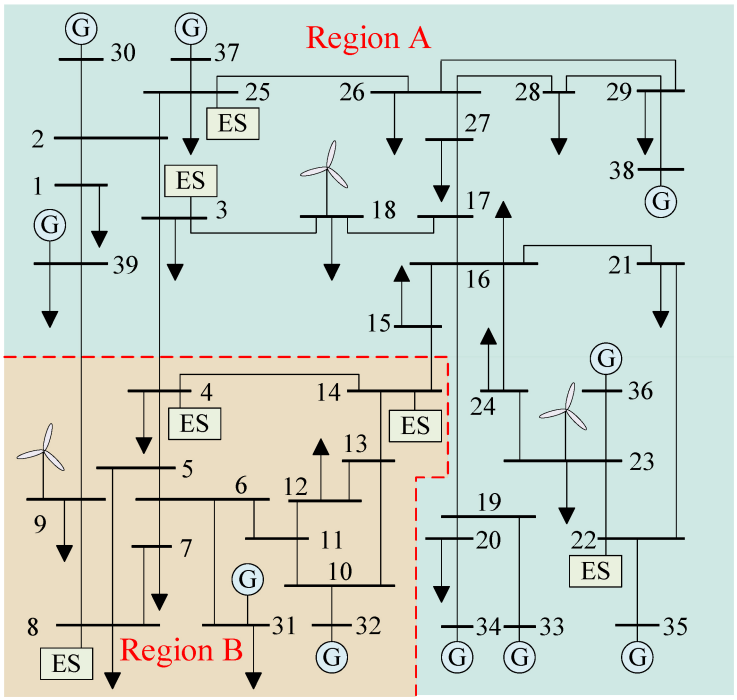


Figure 8. Separated power system after successive failures.

In Equations (A2) and (A3), the expectation value of the Poisson distribution λ is a key parameter. It represents the average rate of occurrences (such as line outages) per unit time. To determine λ precisely, historical data on the frequency of line outages, particularly under specific weather conditions, are required. These data form the basis for a reliable estimate of λ. The calculation of λ involves the following two steps:

(1) Data Collection: Gather historical data on line outages. These data should include the number of outages that occurred over a significant period, along with the duration of each observation period. It is essential to consider the specific weather conditions during which these outages occurred, as λ may vary with different environmental factors.
(2) Calculating the Average Rate: Divide the total number of observed outages by the total observation time to calculate the average rate of outages per unit time. The formula for this calculation is as follows:

$$\lambda = \frac{\text{Total number of outages}}{\text{Total observation time}} \tag{25}$$

After the determination of λ, the probability distribution and probability density function of the lines can be calculated. As a result, Figures 9 and 10 show the probability distribution and probability density function of Line 3–4, Line 9–39, and Line 14–15. Furthermore, the time interval between successive failures is obtained, as shown in Figure 11. Given a confidence level of $1 - \alpha = 0.95$, the failure time of Line 14–15 is calculated as 9:30, the time interval $t_{L,1-\alpha}$ between the successive failures of Line 14–15 and Line 9–39 is calculated as 30 min according to Equation (A7), and the time interval $t_{L,1-\alpha}$ between the successive failures of Line 9–39 and Line 3–4 is calculated as 45 min according to Equation (A7). After the successive failures of Line 14–15, Line 9–39, and Line 3–4, the whole power system is separated into two regions. It is evident that the proposed method accurately predicts the time of the line fault occurrence, with a maximum error not exceeding 3 min in comparison to the actual occurrence. Therefore, the proposed method is capable of providing a relatively precise estimation of the occurrence time of transmission line faults in the power system, thus furnishing essential prospective fault information for subsequent preventive control measures.

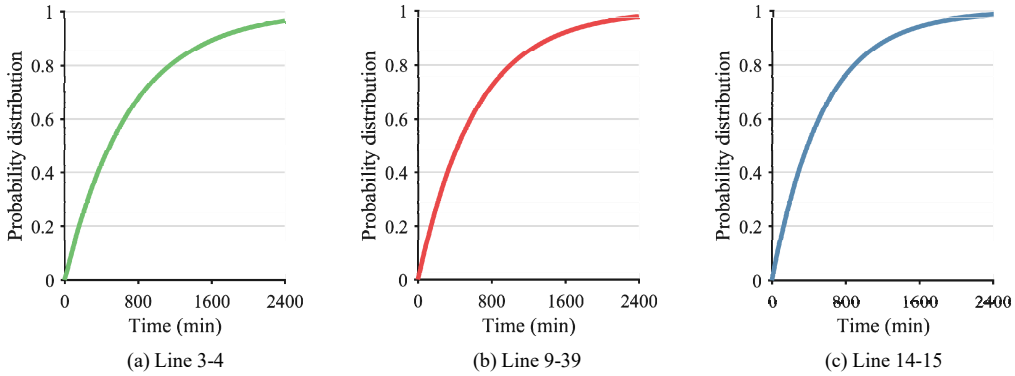


Figure 9. Probability distribution of Line 3–4, Line 9–39, and Line 14–15.

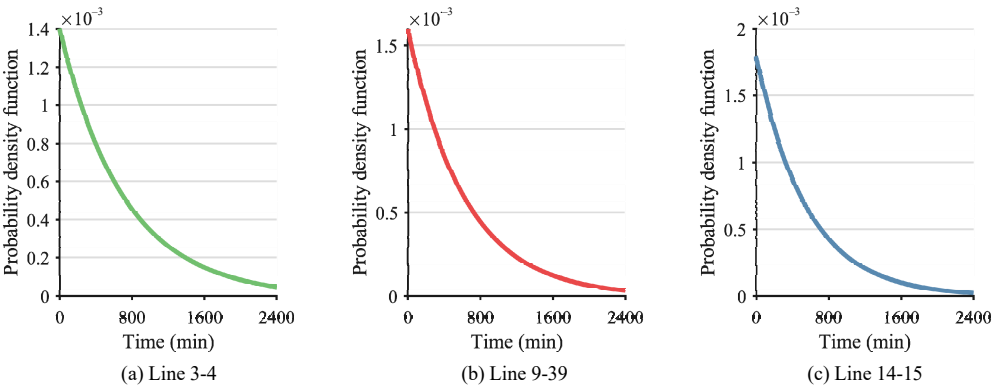
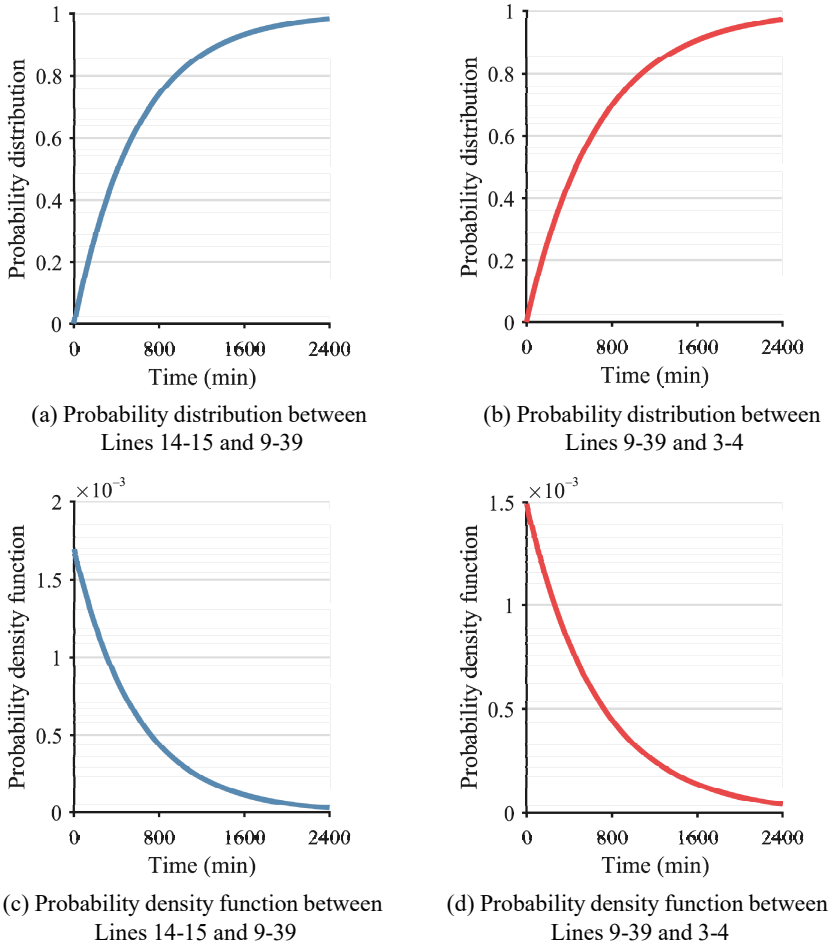


Figure 10. Probability density function of Line 3–4, Line 9–39, and Line 14–15.

Furthermore, based on the predicted fault occurrence time of the line, the method described in Section 2 is applied for the preventive control of the power system, with a time interval of 15 min between adjacent schedules. Figure 12 depicts the output of generators and energy storage units from 9:00 to 10:45, while Figure 13 illustrates the active power flows in the transmission lines connecting Region A and Region B. It is observed that at 9:00, the flow through Line 14–15 remained relatively high, reaching 32.67 MW, whereas at the scheduling time of 9:15, prior to the fault occurrence on Line 14–15, the flow through Line 14–15 had already decreased to 13.46 MW. Consequently, when the fault occurred on Line 14–15 at 9:28, the power system was not significantly affected by the sudden outage of Line 14–15. Furthermore, at various times from 9:00 to 10:30 before the fault occurred on Line 3–4, the proposed method gradually reduced the flow through this line by appropriately scheduling the generators and energy storage, thereby incrementally increasing the output of internal generation resources in Region B. This ensured that, in the event of a sudden fault on Line 3–4, the internal load in Region B could still receive continuous power supply, thereby averting curtailment resulting from the insufficient ramping and adjustment capability of the internal generation resources, thereby avoiding the phenomenon of power limitation within the region. Consequently, the proposed method adequately considers the impact of line faults on the reduced connectivity of the entire power system, proactively adjusting the output of the generators and energy storage units to reduce the power of the transmission lines connecting the two regions, thereby preventing severe oscillations and widespread transfer of power when a line fault occurs, thereby ensuring the continuity and sustainability of the power supply and enhancing the stability and security of power system operations.



(a) Probability distribution between Lines 14-15 and 9-39

(b) Probability distribution between Lines 9-39 and 3-4

(c) Probability density function between Lines 14-15 and 9-39

(d) Probability density function between Lines 9-39 and 3-4

Figure 11. Time interval between successive failures of Lines 3–4 and 9–39 and Lines 9–39 and 14–15.

4.3. Verification of Virtual-Oscillator-Based Lower-Level Control

In this section, we evaluate the efficacy of the subordinate control approach. In order to align with the aforementioned upper-level preventive control outcomes, we considered the dispatch results of the power system at 9:45 as the initial state for subordinate control and conducted the validation of the proposed voltage- and frequency-based lower-level control method using Region B as the test system. Initially, two frequency events are defined, as described below.

Scenario I: The initial active power of the three energy storage units at Nodes 4, 8, and 14 of Region B are 216.03 MW, 226.24 MW, and 310.31 MW, respectively, which are the dispatch results of the power system at 9:45. The output of the wind farm at Node 9 changes from 400 MW to 300 MW suddenly at t = 100 s to emulate the frequency event.

Scenario II: The initial active power of the three energy storage units at Nodes 4, 8, and 14 of Region B are 216.03 MW, 226.24 MW, and 310.31 MW, respectively. The output of the wind farm at Node 9 changes from 300 MW to 335 MW suddenly at t = 100 s to emulate the frequency event.

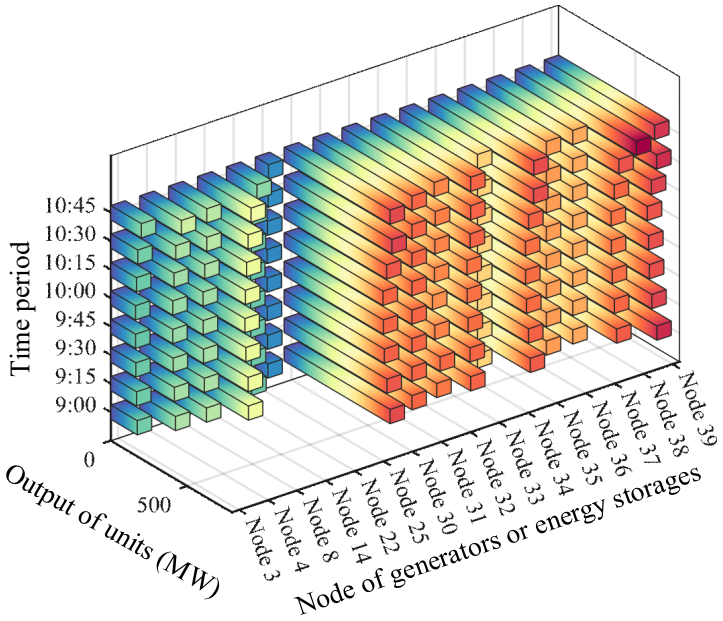


Figure 12. Output of generators and energy storage units in different time periods.

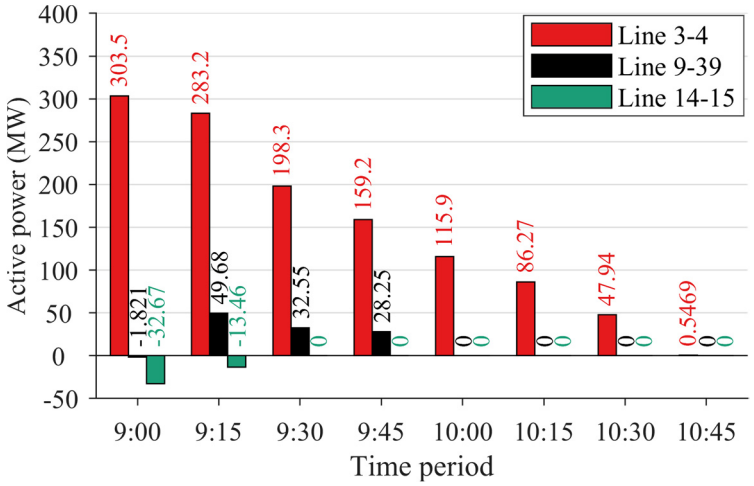


Figure 13. Active power flows in the transmission lines connecting Region A and Region B.

Figure 14 shows the frequency and active power curves of the energy storage units under Scenario I using the proposed lower-level control method. The initial frequency of the microgrid system is 50.00 Hz. Then, the frequency drops dramatically at t = 100 s, and the frequency nadirs for the three energy storage units are about 49.885 Hz, 49.865 Hz, and 49.88 Hz, respectively. The frequency starts to recover after the frequency nadir points, and the frequencies of the three energy storage units are basically the same after the transient dynamic processes. The system frequency recovers to 49.92 Hz, 49.96 Hz, and 50.00 Hz at about t = 101.8 s, t = 104.5 s, and t = 120 s, respectively. As for the active power of the energy storage units, the initial values are 216.03 MW, 226.24 MW, and 310.31 MW, respectively. At t = 100 s, the active power of the energy storage units increases dramatically, and the stable values of the active power for the three energy storage units are about 236 MW, 248 MW, and 340 MW, respectively. Similarly, Figure 15 shows the frequency and active power curves of the energy storage units under Scenario II using the proposed lower-level control method. In this scenario, the initial frequency of the power system is set at 50 Hz. At t = 100 s, the frequency of the three energy storage units suddenly rises to approximately 50.05 Hz. This frequency level, however, is not exceeded, and the frequency then slowly decreases until it returns to the original frequency at around t = 120 s. The active power values of the energy storage units decrease significantly at t = 100 s, and it takes approximately 1 s to stabilize.

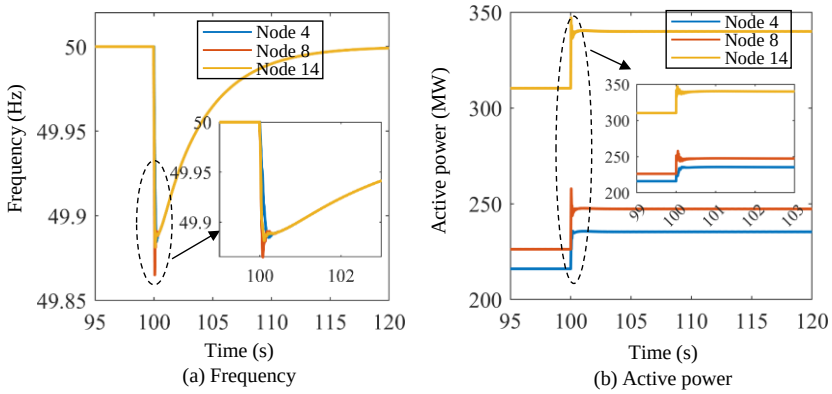


Figure 14. Frequency and active power curves of the energy storage units under Scenario I using the proposed lower-level control method.

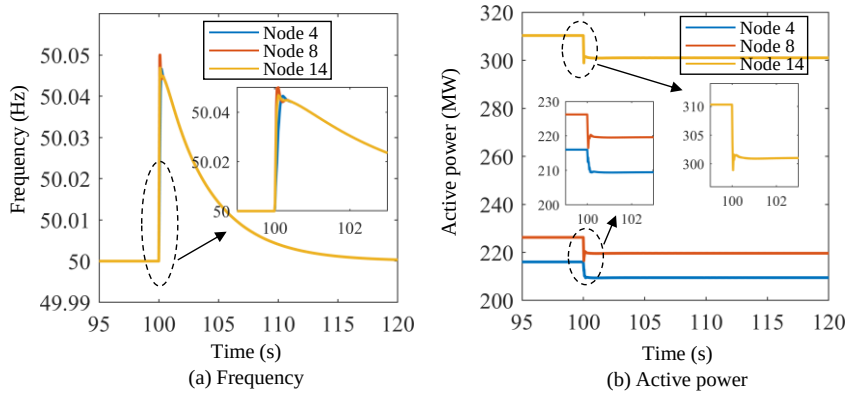


Figure 15. Frequency and active power curves of the energy storage units under Scenario II using the proposed lower-level control method.

Furthermore, this study examines the performance of energy storage in other initial states of lower-level control. Specifically, one frequency event is defined, which is described below.

Scenario III: The initial active power of the three energy storage units at Nodes 4, 8, and 14 of Region B is 246 MW, 200 MW, and 273 MW, respectively. The output of the

wind farm at Node 9 changes from 400 MW to 300 MW suddenly at t = 100 s to emulate the frequency event.

Figure 16 shows the frequency and active power curves of the energy storage units under Scenario III using the proposed lower-level control method. At t = 100 s, the frequency drops sharply and reaches its lowest point. The frequency begins to recover after reaching the lowest frequency, and the three energy storage units basically return to the original frequency at 120 s. The active power of the energy storage units increases significantly and begins to stabilize after increasing to the maximum value. Scenario III exhibits dynamic processes that are strikingly similar to those in Scenario I and Scenario II, indicating that the proposed approach can effectively regulate energy storage in different initial states. Furthermore, the proposed control method yields satisfactory and stable results in variable control experiments.

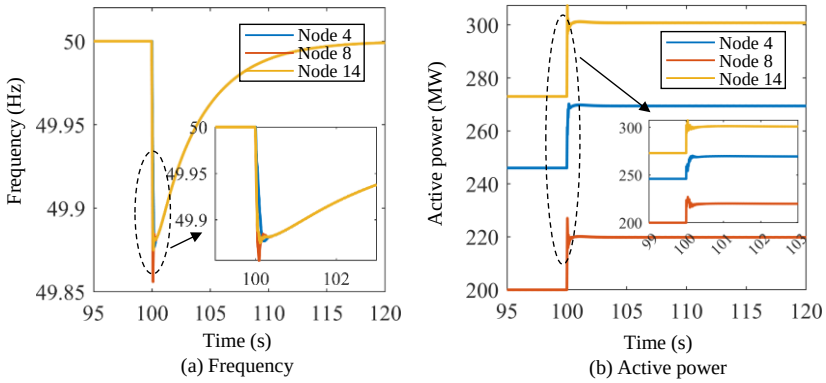


Figure 16. Frequency and active power curves of the energy storage units under Scenario III using the proposed lower-level control method.

4.4. Comparison with Droop Control in Lower-Level Control

The output characteristics of the traditional converters of the energy storage units generally simulate the characteristics of a synchronous generator. Depending on the degree of accuracy of the simulation of the synchronous generator, the most representative ones are droop control and VSG control. In order to analyze the difference between the VOC strategy and a traditional control strategy, the droop control strategy has been selected as the compared method in this paper. Droop control is designed to simulate the steady-state droop characteristics of a synchronizer and is a type of proportional control in the phasor domain. Droop control serves as a pertinent comparison to VOC due to its contrasting approach. Characterized by decentralized control, simplicity, and proven performance under varied conditions, droop control serves as a robust benchmark to evaluate the advanced capabilities of VOC. This comparison is instrumental in highlighting the advantages of VOC, such as faster response, enhanced stability, and adaptability to modern grid demands.

In the simulation example, the VOC strategy of the energy storage units in Figure 6 is replaced with the droop control strategy. Meanwhile, considering the differences between the VOC strategy and the droop control strategy, the role of the sparse communication network in the coordination between the VOC strategy and the droop control strategy is temporarily ignored in this paper. That is, when the communication network is removed, all of the energy storage units adopt local control. To compare the VOC strategy and droop control strategy, Scenario IV and Scenario V, described below, were selected to test the two controllers.

Figures 17 and 18 show the active power curves of the energy storage units under Scenario I using both methods. Figures 19 and 20 show the frequency and active power curves of the energy storage units under Scenario II using both methods. By comparing the simulation results, it can be seen that the change process of frequency and active power in the VOC strategy are much faster than those in the droop control strategy. Additionally,

the droop control strategy takes a longer time to return to the new stable value, and the maximum overshoot and adjustment time are significantly greater than those of the VOC strategy. Taking Figures 17 and 18 as an example, the VOC strategy is able to stabilize the frequency within 2 s, in contrast to the droop control strategy, where the frequency remains fluctuating even after 20 s of adjustment. Moreover, the VOC strategy effectively avoids overshooting during the adjustment process. As illustrated in Figure 17, under the VOC strategy, the steady-state frequency is approximately 49.85 Hz, with the lowest frequency point being slightly below 49.85 Hz. In contrast, as shown in Figure 18, with the droop control strategy, the system's frequency fluctuates within a range of about 49.5 Hz to 50.15 Hz, indicating a lower stability in frequency control. This comparison highlights the superior performance of the VOC strategy in maintaining frequency stability and preventing excessive fluctuations, making it a more efficient and reliable control method for power systems.

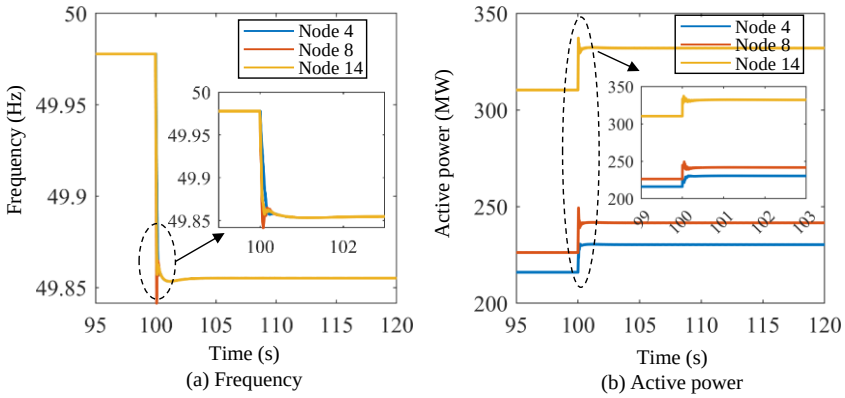


Figure 17. Frequency and active power curves of the energy storage units under Scenario I using the proposed lower-level control method without the communication network.

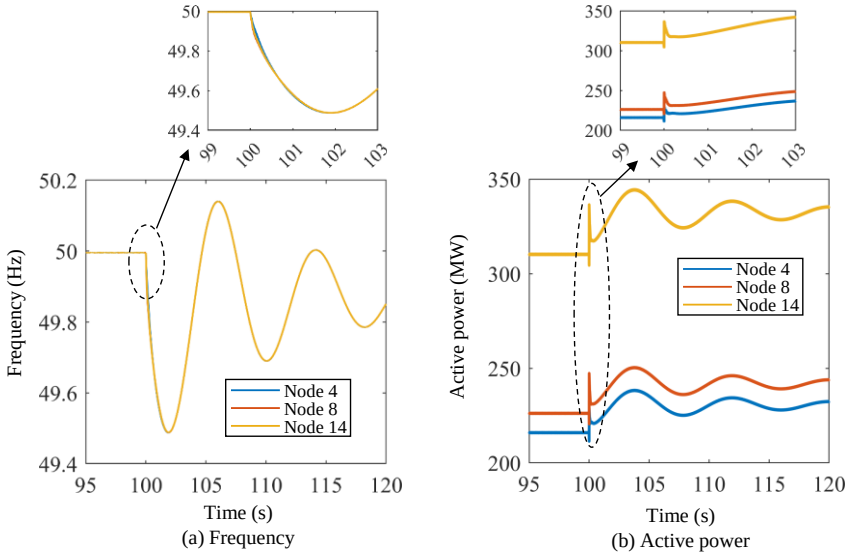


Figure 18. Frequency and active power curves of the energy storage units under Scenario I using the droop-based primary frequency control method.

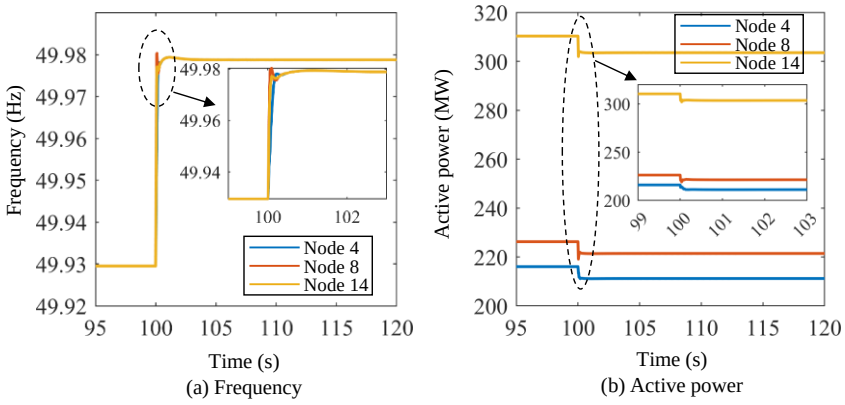


Figure 19. Frequency and active power curves of the energy storage units under Scenario II using the proposed lower-level control method without the communication network.

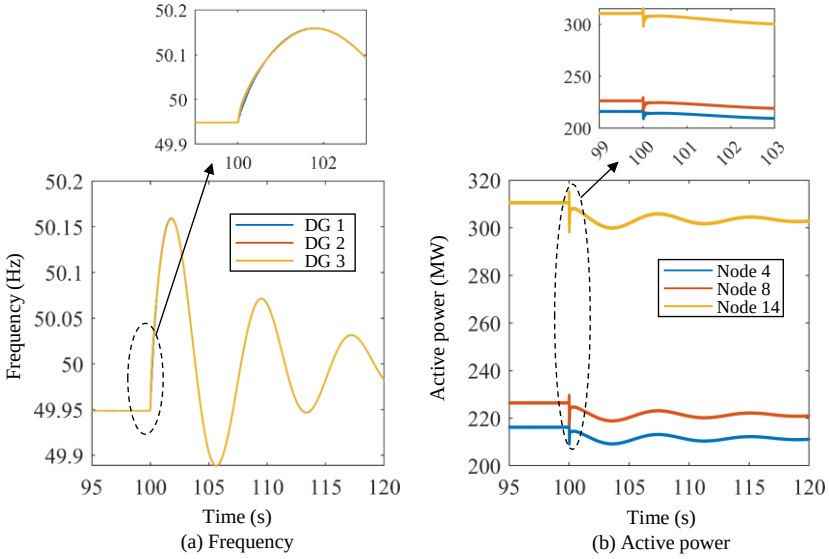


Figure 20. Frequency and active power curves of the energy storage units under Scenario II using the droop-based primary frequency control method.

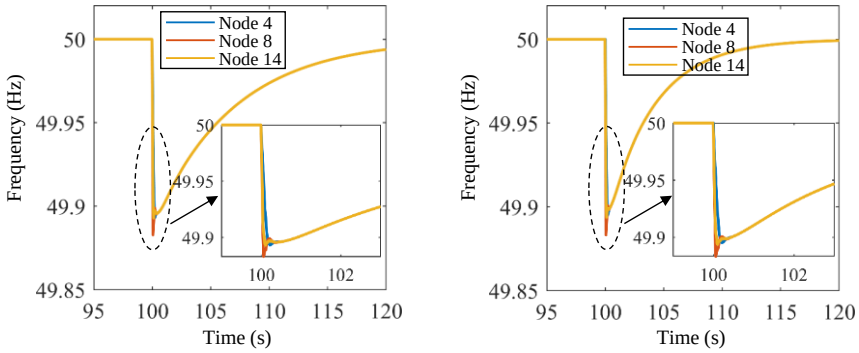
4.5. Influence of the Adaptive Control Parameters in Lower-Level Control

In this paper, an adaptive frequency regulation method with variable parameters is proposed. To clearly capture the indicators measuring the inertial frequency regulation response with different selections of parameters, the frequencies under Scenario IV and Scenario V, described below, using fixed control parameters and adaptive control parameters are compared.

Scenario IV: The initial active power of the three energy storage units at Nodes 4, 8, and 14 of Region B is 216.03 MW, 226.24 MW, and 310.31 MW, respectively. The output of the wind farm at Node 9 changes from 400 MW to 332 MW suddenly at t = 100 s to emulate the frequency event.

Scenario V: The initial active power of the three energy storage units at Nodes 4, 8, and 14 of Region B is 216.03 MW, 226.24 MW, and 310.31 MW, respectively. The output of the wind farm at Node 9 changes from 300 MW to 345 MW suddenly at t = 100 s to emulate the frequency event.

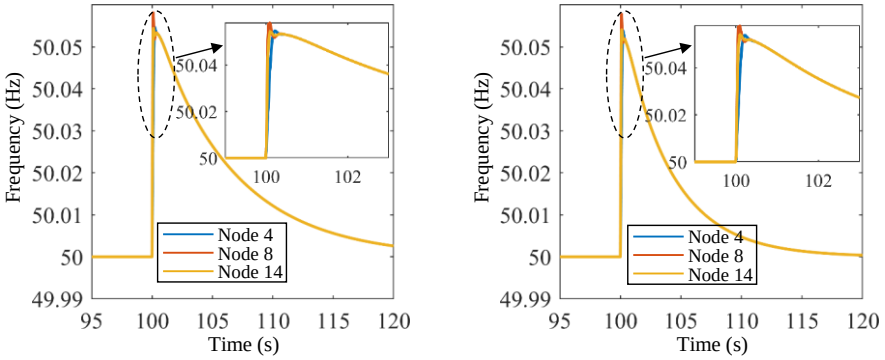
Figure 21 shows the frequency curves under Scenario IV using the fixed control parameters and the adaptive control parameters. Figure 22 shows the frequency curves under Scenario V using the fixed control parameters and the adaptive control parameters.



(a) Frequency curve using the fixed control parameters

(b) Frequency curve using the adaptive control parameters

Figure 21. Frequency curves under Scenario IV using the fixed control parameters and the adaptive control parameters.



(a) Frequency curve using the fixed control parameters

(b) Frequency curve using the adaptive control parameters

Figure 22. Frequency curves under Scenario V using the fixed control parameters and the adaptive control parameters.

It can be observed that both the VOC controllers with fixed and adaptive control parameters enter the transient process at the same time. However, the performance of these two control strategies differs significantly. VOC with adaptive control parameters is able to restore the rated frequency in a shorter period compared to the VOC controller with fixed control parameters. Specifically, the VOC controller with adaptive control parameters takes about 15~20 s to restore the rated frequency, while the VOC controller with fixed control parameters takes much longer. This suggests that the adaptive virtual inertia control strategy is more effective than the traditional VOC strategy in regulating the frequency of the power system. Through the incorporation of virtual inertia elements into the control strategy, VOC controllers with adaptive control parameters are able to respond faster to changes in power fluctuations, resulting in a shorter adjustment time in the frequency response. This advantage is particularly pronounced under transient conditions when the system experiences sudden changes in power demand or supply.

5. Conclusions

This paper develops a multi-level operation method for improving the resilience of power systems under extreme weather conditions by incorporating preventive control and virtual oscillator (VO) technology. The method's ability to precisely estimate the occurrence time of transmission line faults is a significant advancement, enabling the implementation of effective preventive controls. By considering the impact of line faults on system connectivity, the method proactively adjusts the output of generators and energy storage units, effectively reducing the power in transmission lines and preventing severe oscillations during faults. This ensures the continuity and sustainability of the power supply, thereby enhancing the overall stability and security of power system operations. In addition, the method

demonstrates robust performance in regulating energy storage under various conditions and shows superior stability and speed in control experiments, particularly highlighting the effectiveness of VOC over traditional droop control. Specifically, compared with droop control, VOC demonstrates the ability to stabilize frequency more quickly, effectively avoids overshooting during the adjustment process, and achieves greater stability in frequency control. These results emphasize the method's potential as a comprehensive solution for enhancing power system resilience in the face of increasing extreme weather events.

Although the proposed multi-level operation method enhances the resilience of power systems, we must admit that there are challenges in ensuring the stability of adaptive VOC under all possible circumstances. Specifically, our approach may struggle in situations like the tripping of a major generating station. To address this issue, future work could explore new control strategies to improve the system's adaptability and resilience to sudden events. This could include the development of more advanced predictive models capable of the real-time monitoring and prediction of the behavior of power systems and the automatic adjustment of the VOC strategy upon detecting potential instability signals. For example, by integrating machine learning, it would be possible to design control systems that learn from past failure events and quickly adapt to new scenarios.

Author Contributions: Conceptualization, J.H.; data curation, L.X.; formal analysis, C.L., C.T. and G.Z.; investigation, Z.F.; methodology, C.L., D.Z., J.H., L.L. and G.Z.; software, J.H. and C.W.; validation, L.X.; writing—original draft, J.H. and L.X.; writing—review and editing, J.H. and C.W. All authors have read and agreed to the published version of the manuscript.

Funding: This research received no external funding.

Data Availability Statement: Data are contained within the article.

Conflicts of Interest: The authors declare no conflicts of interest.

Appendix A. Modeling of Successive Failures in Power Systems

Under extreme weather conditions, the failure probability of a transmission line can be expressed using a Poisson model. This is because the Poisson model is a tool for characterizing stochastic and rare occurrences of events. In extreme weather conditions, the occurrence of transmission line faults may exhibit stochastic and rare characteristics. The Poisson model is well suited to capturing this stochastic and rare behavior with a certain degree of accuracy [30,31] and is therefore employed to describe the probability of transmission line faults under extreme weather conditions. Given a specific extreme weather event, the probability of a single-component failure, taking a line outage as an example, is described by a Poisson model as follows [32]:

$$\begin{cases} P(X=k) = \frac{\lambda^k}{k!} e^{-\lambda} \\ E(X) = \lambda \end{cases} \tag{A1}$$

where k represents the number of line failures; λ is the expectation value of the Poisson distribution.

Subsequently, we can formulate the Poisson process using the above as follows:

$$P(X(t)=k) = \frac{(\lambda t)^k}{k!} e^{-\lambda t} \tag{A2}$$

where $P(X(t)=k)$ is the probability of k line outages in a time period $(0, A)$.

Let Y be the time interval between the kth and $k+1$th trips. The probability distribution and probability density function of Y are

$$P(Y \le t) = 1 - P(Y > t) = 1 - P(X(t)=0) = 1 - e^{-\lambda t} \tag{A3}$$

$$p(t) = \begin{cases} \lambda e^{-\lambda t} & t \geq 0 \\ 0 & t < 0 \end{cases} \tag{A4}$$

Let t_i and t_j be the tripping time of two lines; then, their probability density functions are

$$f_1(t) = \begin{cases} \lambda_1 e^{-\lambda_1 t} & t \geq 0 \\ 0 & t < 0 \end{cases} \tag{A5}$$

$$f_2(t) = \begin{cases} \lambda_2 e^{-\lambda_2 t} & t \geq 0 \\ 0 & t < 0 \end{cases} \tag{A6}$$

Then, the probability density function of the time interval between t_i and t_j, which is $t = t_i - t_j$, can be written as

$$f(t) = \int_{-\infty}^{+\infty} f(x, x-t)dx = \int_{-\infty}^{+\infty} f_1(x) f_2(x-t)dx = \begin{cases} \frac{\lambda_1\lambda_2}{\lambda_1+\lambda_2} e^{\lambda_2 t} & t < 0 \\ \frac{\lambda_1\lambda_2}{\lambda_1+\lambda_2} e^{-\lambda_1 t} & t \geq 0 \end{cases} \tag{A7}$$

Further, the probability density function and probability distribution of $|t|$ are

$$f(|t|) = \frac{\lambda_1\lambda_2}{\lambda_1+\lambda_2}\left(e^{-\lambda_1 t} + e^{-\lambda_2 t}\right) \tag{A8}$$

$$F(|t|) = 1 - \frac{\lambda_2}{\lambda_1+\lambda_2} e^{-\lambda_1 t} - \frac{\lambda_1}{\lambda_1+\lambda_2} e^{-\lambda_2 t} \tag{A9}$$

Utilizing the interval estimation technique, one can determine the prediction interval for the duration between two line failures $[t_{L,1-\alpha}, t_{U,1-\alpha}]$ with a confidence level set at $1-\alpha$. Herein, $t_{L,1-\alpha}$ serves as the gap between failures.

Appendix B. The Influence of VOC Parameters on Transient Characteristics

This part focuses on how the VOC parameters affect the inverter output transient process. The transient process refers to the flow of energy between the energy storage element and resistance. As such, it is predominantly influenced by the circuit's initial energy, structure, and the parameters of the circuit elements, rather than external signals like the power supply. This means that the circuit structure can be simplified and analyzed with greater accuracy. To achieve this simplification, the circuit model of VOC is represented as a second-order circuit in parallel with RLC without power excitation, as shown in Figure A1.

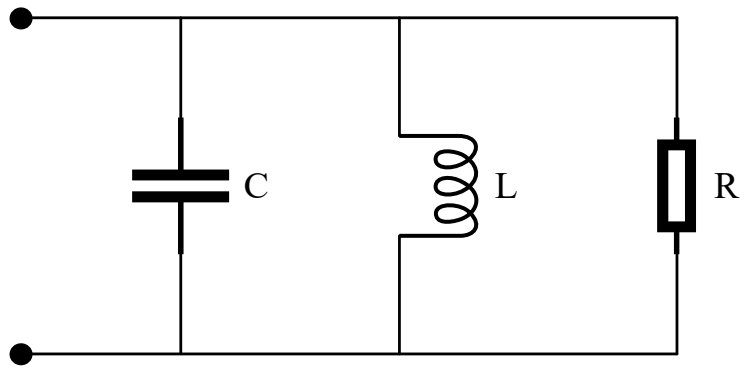


Figure A1. Simplified RLC parallel circuit.

When $i_L(0_-) = I_{L0} > 0$, the switch is set to "on" at t = 0 s. According to circuit theory, one can obtain

$$\frac{\mathrm{d}^2 i_L}{\mathrm{d}t^2} - \frac{1}{RC}\frac{\mathrm{d}i_L}{\mathrm{d}t} + \frac{1}{LC} i_L = 0 \tag{A10}$$

with the initial conditions

$$\begin{array}{l} i_L(0_-) = i_L(0_+) = I_{L0} \\ \left.\frac{\mathrm{d}i_L}{\mathrm{d}t}\right|_{t=0_+} = \frac{1}{L}u(0_+) = \frac{1}{L}u(0_-) = 0 \end{array} \tag{A11}$$

Suppose that the circuit has a zero-input response; that is, the forced component of u_c is zero, and the characteristic equation and characteristic root of the differential equation are

$$p^2 - \frac{1}{RC}p + \frac{1}{LC} = 0 \tag{A12}$$

$$p = \frac{1}{2RC} \pm \sqrt{\left(\frac{1}{2RC}\right)^2 - \frac{1}{LC}} \tag{A13}$$

Let $\gamma = 1/(2RC)$ and $\omega^* = 1/\sqrt{LC}$; the two root characteristics can be expressed as

$$\begin{cases} p_1 = \gamma + \sqrt{\gamma^2 - (\omega^*)^2} \\ p_2 = \gamma - \sqrt{\gamma^2 - (\omega^*)^2} \end{cases} \tag{A14}$$

The above formula shows that the characteristic roots p_1 and p_2 are determined by the component parameters in the circuit ($R < 0, L > 0, C > 0$). p_1 and p_2 can be double roots, distinct real roots, or conjugate complex roots. In order to explore the influence of circuit parameters on the transient process, it is necessary to derive the time constant of the transient component.

Condition 1: Let $|\gamma| > |\omega^*|$; the circuit structure parameters would satisfy $R > -0.5\lambda$. In this circumstance, p_1 and p_2 are two different negative real roots, and the general solution of the equation is $i_L = A_1 \mathrm{e}^{p_1 t} + A_2 \mathrm{e}^{p_2 t}$. With the initial conditions, one can obtain

$$\begin{cases} A_1 = \frac{p_2}{p_2 - p_1} I_{L0} \\ A_2 = -\frac{p_1}{p_2 - p_1} I_{L0} \end{cases} \tag{A15}$$

It is obvious that $A_1 > 0, A_2 < 0, |A_1| > |A_2|$, and we can know from (A13) that $p_1 < 0, p_2 < 0, |p_1| < |p_2|$.

Condition 2: Let $|\gamma| = |\omega^*|$; the circuit structure parameters would satisfy $R = -0.5\lambda$. In this circumstance, p_1 and p_2 are equal and are the negative real roots, and the circuit is in a state between that with oscillations and that without oscillations.

Condition 3: Let $|\gamma| < |\omega^*|$; the circuit structure parameters would satisfy $R < -0.5\lambda$. In this circumstance, p_1 and p_2 are a pair of conjugate complex roots, and the general solution of the equation is $i_L = A\mathrm{e}^{\gamma t}\sin(\omega_d t + \theta)$. This circuit is a process of vibration attenuation, and the attenuation rate is determined by the attenuation coefficient γ; also, the time constant is $\tau = -1/\gamma$.

In view of the above three conditions, the transient process of Condition 3 is the wanted oscillating structure, and the time constant is $\tau = -1/\gamma$. Because the rated angular frequency ω^* is constant, the time constant τ is inversely proportional to γ. In other words, τ is proportional to C.

Through considering Condition 3, we know that a small $\lambda \searrow 0$ results in a nearly sinusoidal output voltage in the steady state with a lower frequency deviation from the nominal value ω^* and reduced harmonic content in the output terminal voltage. However, a small $\lambda \searrow 0$ slows down the dynamic response of the VOC inverter. Therefore, in the design of VOC parameters, the control parameters L and C should be reasonably designed according to the control requirements. The design principles of L and C are

$$\begin{cases} \max\left\{C^{\min}_{|\Delta\omega|_{\max}}, C^{\min}_{\delta_{3:1}}\right\} \le C \le C^{\max}_{t_{\text{rise}}} \\ L = \frac{1}{C(\omega^*)^2} \end{cases} \tag{A16}$$

$$\begin{cases} C^{\min}_{|\Delta\omega|_{\max}} = \frac{1}{2|\Delta\omega|_{\max}} \frac{\overline{V}_{oc}}{\overline{V}_{\min}} \frac{|\overline{Q}_{rated}|}{\overline{P}_{rated}} \\ C^{\max}_{t_{rise}} = \frac{t^{\max}_{rise}}{6} \frac{\overline{V}_{oc}}{\overline{V}_{\min}} \frac{\overline{V}^2_{oc}}{\overline{V}^2_{oc} - \overline{V}^2_{\min}} \\ C^{\min}_{\delta_{3:1}} = \left(\frac{1}{8\omega^* \delta^{\max}_{3:1}}\right) \frac{\overline{V}_{oc}}{\overline{V}_{\min}} \frac{\overline{V}^2_{oc}}{\overline{V}^2_{oc} - \overline{V}^2_{\min}} \end{cases} \quad \text{(A17)}$$

where $t^{\max}_{rise}$ is the maximum permissible rise time. $\delta^{\max}_{3:1}$ is the maximum permissible ratio. $\overline{V}_{oc}$ is the open-circuit voltage. $\overline{P}_{rated}$ is the rated real power. $\overline{V}_{\min}$ is the voltage at the rated power. $\overline{Q}_{rated}$ is the rated reactive power. $|\Delta\omega|_{\max}$ is the maximum frequency offset. $t^{\max}_{rise}$ is the rise time. $\delta^{\max}_{3:1}$ is the ratio of the third-to-first harmonic.

It can be seen that the optimal parameters of VOC are affected by the operating state of the system, and it is necessary to adjust the VOC parameters in a timely manner according to the changes in the operating state of the system to achieve the optimal frequency regulation performance. It should be noted that Formula (A14) only provides the adjustment ranges of L and C, without determining the optimal control parameters. Therefore, an adaptive multi-level frequency regulation method and VOC parameter design method are proposed.

References

1. Han, J.; Lyu, W.; Song, H.; Qu, Y.; Wu, Z.; Zhang, X.; Li, Y.; Chen, Z. Optimization of Communication Network for Distributed Control of Wind Farm Equipped with Energy Storages. *IEEE Trans. Sustain. Energy* **2023**, *14*, 1933–1949. [CrossRef]
2. Pan, W.; Li, Y. Improving Power Grid Resilience Under Extreme Weather Conditions With Proper Regulation and Management of DERs—Experiences Learned From the 2021 Texas Power Crisis. *Front. Energy Res.* **2022**, *10*, 921335. [CrossRef]
3. Bie, Z.; Lin, Y.; Qiu, A. Concept and Research Prospects of Power System Resilience. *Autom. Electr. Power Syst.* **2015**, *39*, 1–9.
4. Roege, P.E.; Collier, Z.A.; Mancillas, J.; McDonagh, J.A.; Linkov, I. Metrics for energy resilience. *Energy Policy* **2014**, *72*, 249–256. [CrossRef]
5. Panteli, M.; Mancarella, P.; Trakas, D.N.; Kyriakides, E.; Hatziargyriou, N.D. Metrics and Quantification of Operational and Infrastructure Resilience in Power Systems. *IEEE Trans. Power Syst.* **2017**, *32*, 4732–4742. [CrossRef]
6. Reed, D.A.; Kapur, K.C.; Christie, R.D. Methodology for Assessing the Resilience of Networked Infrastructure. *IEEE Syst. J.* **2009**, *3*, 174–180. [CrossRef]
7. Mahzarnia, M.; Moghaddam, M.P.; Baboli, P.T.; Siano, P. A Review of the Measures to Enhance Power Systems Resilience. *IEEE Syst. J.* **2020**, *14*, 4059–4070. [CrossRef]
8. Arjomandi-Nezhad, A.; Fotuhi-Firuzabad, M.; Moeini-Aghtaie, M.; Safdarian, A.; Dehghanian, P.; Wang, F. Modeling and Optimizing Recovery Strategies for Power Distribution System Resilience. *IEEE Syst. J.* **2021**, *15*, 4725–4734. [CrossRef]
9. Yan, M.; Ai, X.; Shahidehpour, M.; Li, Z.; Wen, J.; Bahramira, S.; Paaso, A. Enhancing the Transmission Grid Resilience in Ice Storms by Optimal Coordination of Power System Schedule with Pre-Positioning and Routing of Mobile DC DE-Icing Devices. *IEEE Trans. Power Syst.* **2019**, *34*, 2663–2674. [CrossRef]
10. Noebels, M.; Quirós-Tortós, J.; Panteli, M. Decision-Making Under Uncertainty on Preventive Actions Boosting Power Grid Resilience. *IEEE Syst. J.* **2022**, *16*, 2614–2625. [CrossRef]
11. Nazemi, M.; Moeini-Aghtaie, M.; Fotuhi-Firuzabad, M.; Dehghanian, P. Energy Storage Planning for Enhanced Resilience of Power Distribution Networks Against Earthquakes. *IEEE Trans. Sustain. Energy* **2020**, *11*, 795–806. [CrossRef]
12. Karim, M.A.; Currie, J.; Lie, T.T. Distributed Machine Learning on Dynamic Power System Data Features to Improve Resiliency for the Purpose of Self-Healing. *Energies* **2020**, *13*, 3494. [CrossRef]
13. Kamruzzaman, M.; Duan, J.; Shi, D.; Benidris, M. A Deep Reinforcement Learning-based Multi-Agent Framework to Enhance Power System Resilience using Shunt Resources. *IEEE Trans. Power Syst.* **2021**, *36*, 5525–5536. [CrossRef]
14. Musleh, A.S.; Khalid, H.M.; Muyeen, S.M.; Al-Durra, A. A Prediction Algorithm to Enhance Grid Resilience Toward Cyber Attacks in WAMCS Applications. *IEEE Syst. J.* **2019**, *13*, 710–719. [CrossRef]
15. Wang, Y.; Huang, L.; Shahidehpour, M.; Lai, L.L.; Yuan, H.; Xu, F.Y. Resilience-Constrained Hourly Unit Commitment in Electricity Grids. *IEEE Trans. Power Syst.* **2018**, *33*, 5604–5614. [CrossRef]
16. Liu, X.; Shahidehpour, M.; Li, Z.; Liu, X.; Cao, Y.; Bie, Z. Microgrids for Enhancing the Power Grid Resilience in Extreme Conditions. *IEEE Trans. Smart Grid* **2017**, *8*, 589–597.
17. Wang, F.; Chen, C.; Li, C.; Cao, Y.; Li, Y.; Zhou, B.; Dong, X. A Multi-Stage Restoration Method for Medium-Voltage Distribution System With DGs. *IEEE Trans. Smart Grid* **2017**, *8*, 2627–2636. [CrossRef]
18. Dehghanian, P.; Aslan, S.; Dehghanian, P. Quantifying Power System Resilience Improvement Using Network Reconfiguration. In Proceedings of the IEEE 60th International Midwest Symposium on Circuits and Systems (MWSCAS), Boston, MA, USA, 6–9 August 2017; pp. 1558–3899.
19. Huang, G.; Wang, J.; Chen, C.; Qi, J.; Guo, C. Integration of Preventive and Emergency Responses for Power Grid Resilience Enhancement. *IEEE Trans. Power Syst.* **2017**, *32*, 4451–4463. [CrossRef]

20. Li, Q.; Zhang, X.; Guo, J.; Shan, X.; Wang, Z.; Li, Z.; Tse, C.K. Integrating Reinforcement Learning and Optimal Power Dispatch to Enhance Power Grid Resilience. In *IEEE Transactions on Circuits and Systems II: Express Briefs*; IEEE: Piscataway, NJ, USA, 2021; Volume 69, pp. 1402–1406.
21. Wei, X.; Liang, Y.; Guo, L.; Zhang, D.; Jia, Y. Research on fault location method of distribution network based on Lambda algorithm. *Electr. Meas. Instrum.* **2022**, *59*, 71–76.
22. Duanmu, J.C.; Yuan, Y. Calculation method of outage probability of distribution network based on real-time failure rate of equipment. *Electr. Meas. Instrum.* **2023**, *60*, 26–32.
23. Zhang, L.; Dou, X.; Zhao, W.; Hu, M. Islanding detection for active distribution network considering demand response. *Electr. Meas. Instrum.* **2019**, *56*, 63–68; 75.
24. Lu, M.; Dhople, S.; Johnson, B. Benchmarking Nonlinear Oscillators for Grid-Forming Inverter Control. *IEEE Trans. Power Electron.* **2022**, *37*, 10250–10266. [CrossRef]
25. Lu, M. Virtual Oscillator Grid-Forming Inverters: State of the Art, Modeling, and Stability. *IEEE Trans. Power Electron.* **2022**, *37*, 11579–11591. [CrossRef]
26. Nguyen, N.; Almasabi, S.; Bera, A.; Mitra, J. Optimal power flow incorporating frequency security constraint. *IEEE Trans. Ind. Appl.* **2019**, *55*, 6508–6516. [CrossRef]
27. Hao, Z.; Guo, G.; Huang, H. A Particle Swarm Optimization Algorithm with Differential Evolution. In Proceedings of the 2007 International Conference on Machine Learning and Cybernetics, Hong Kong, China, 19–22 August 2007; pp. 1031–1035. [CrossRef]
28. Mazumder, S.K.; Greidanus, M.D.R.; Liu, J.; Mantooth, H.A. Vulnerability of a VOC-Based Inverter Due to Noise Injection and Its Mitigation. *IEEE Trans. Power Electron.* **2022**, *38*, 1445–1450. [CrossRef]
29. Johnson, B.B.; Sinha, M.; Ainsworth, N.G.; Dorfler, F.; Dhople, S.V. Synthesizing virtual oscillators to control islanded inverters. *IEEE Trans. Power Electron.* **2015**, *31*, 6002–6015. [CrossRef]
30. Wang, J.; Heydt, G.T. Application of Poisson models to electric power system reliability evaluation. *IEEE Trans. Power Syst.* **2006**, *21*, 1493–1500.
31. Hu, Y.; Wang, W.; Liu, Y. Short-term load forecasting using a hybrid model based on Poisson regression and artificial neural network. *Appl. Energy* **2017**, *185*, 1491–1500.
32. Zhang, Z.; Cui, W.; Niu, S.; Wang, C.; Xue, C.; Ma, X.; Liu, S.; Bie, Z. Preventive control of successive failures in extreme weather for power system resilience enhancement. *IET Gener. Transm. Distrib.* **2022**, *16*, 3245–3255. [CrossRef]

Disclaimer/Publisher's Note: The statements, opinions and data contained in all publications are solely those of the individual author(s) and contributor(s) and not of MDPI and/or the editor(s). MDPI and/or the editor(s) disclaim responsibility for any injury to people or property resulting from any ideas, methods, instructions or products referred to in the content.